Research Article

OPTICA

Non-classical optimization of entangled photons through complex media

Baptiste Courme,[1,2,*] Chloé Vernière,[1] Malo Joly,[2] Daniele Faccio,[3] Sylvain Gigan,[2] and Hugo Defienne[1]

[1]Sorbonne Université, CNRS, Institut des NanoSciences de Paris, INSP, Paris F-75005, France
[2]Laboratoire Kastler Brossel, ENS-Universite PSL, CNRS, Sorbonne Universite, College de France, 24 rue Lhomond, Paris 75005, France
[3]School of Physics and Astronomy, University of Glasgow, Glasgow, G12 8QQ, UK
*baptiste.courme@lkb.ens.fr

Received 12 November 2025; revised 27 February 2026; accepted 18 March 2026; published 18 May 2026

Optimization approaches are ubiquitous in physics. In optics, they are key to manipulating light through complex media, enabling applications ranging from imaging to photonic simulators. In most demonstrations, however, the optimization process is implemented using classical coherent light, leading to a purely classical solution. Here, we introduce the concept of optical non-classical optimization in complex media. We experimentally demonstrate the control and refocusing of non-classical light—namely, entangled photon pairs—through a scattering medium by directly optimizing the output coincidence rate. Importantly, these optimal solutions cannot be obtained with classical light and do not result in a focus for classical light; this is a result of entanglement in the input state. This genuinely non-classical optimization method promises advances in quantum imaging, communication, and optical simulations with non-classical light.

https://doi.org/10.1364/OPTICA.583959

1. INTRODUCTION

In 2007, Vellekoop and Mosk demonstrated the focusing of classical coherent light through opaque scattering media [1]. They developed an optimization process that tailors the wavefront of a coherent beam incident on the medium using a spatial light modulator (SLM), based on a speckle intensity feedback measured by a camera behind it [Figs. 1(a)–1(d)]. Two decades later, this breakthrough has led to numerous applications in deep-tissue imaging [2,3], light transport in multimode fibers [4], optical trappings [5], and complex problems simulation [6,7]. In recent years, it was also extended to quantum optics [8]. Pioneering studies have, for example, reported the focusing of single photons and photon pairs through thick scattering media [9–11] and multimode fibers [12,13]. These approaches have subsequently been applied to more practical scenarios, such as programming quantum circuits [14–16], imaging through optical aberrations [17], and restoring entanglement after transmitting photons through fibers [18], scattering layers [19–22], and turbulent atmosphere [23–25].

Although all these studies involve non-classical optical states, they still rely on classical wavefront shaping. Indeed, in most of them, wavefront optimization is performed first using a classical light source—a laser aligned in the same direction as the quantum state, sharing similar spectral and polarization properties—before applying the optimal solution to the quantum signal. This method benefits from an intense signal for optimization, which is particularly useful in high-loss scenarios (e.g., multiple scattering) and dynamic conditions (e.g., turbulence) [1,26,27]. However, it completely ignores the non-classical features of the quantum state involved, making the process purely classical.

Ignoring the quantum state's specifics in the shaping process has its limits. Practically, ensuring perfect mode matching between a classical and a non-classical source is often challenging. For example, in the context of high-dimensional entangled states, such as spatially entangled photon pairs [28], scattering has only been corrected either simultaneously for a small subset of modes [20,21,29] or sequentially by addressing each mode individually [15,18]. More importantly, it fundamentally restricts the efficiency and range of the control achieved. Purely non-classical phenomena, such as complex quantum interference [16,30] and entanglement scrambling [18,21], for example, are not taken into account when using classical optimization.

Here, we present an optimization-based wavefront shaping method with direct feedback from a non-classical feature of a quantum state, leading to solutions unattainable through classical optimization—a method we refer to as "non-classical optimization." Our experimental implementation involves an entangled two-photon state propagating through a scattering medium. Contrary to previous works, the feedback signal is derived directly from photon coincidence measurements across spatial modes at the output, which are specific to the non-classical source. To better understand this behavior, we investigate the two-photon interference processes occurring in the scattering medium and

develop an analytical model for the spatial correlation modulation. We demonstrate that the optimization converges towards unique solutions, which do not refocus classical light. Crucially, we show that these non-classical solutions exist and are accessible only if entanglement is present between the photons. Finally, we discuss the potential of this non-classical optimization approach beyond imaging and communication such as in solving complex spin-glass optimization problems.

2. CONCEPT

Figure 1 conceptually compares classical and non-classical optimization. A non-classical state propagates through a complex medium and is measured at the output by a detector sensitive to its quantum properties such as a single-photon or homodyne detector. A feedback mechanism is then implemented, linking this measurement to a programmable device that shapes the properties of the state incident on the medium. An iterative algorithm adjusts the input (usually the spatial phase pattern) toward a configuration that optimizes the targeted non-classical property.

In our work, non-classical optimization is demonstrated using a spatially entangled two-photon state propagating through a scattering layer and detected by a single-photon avalanche diode (SPAD) camera. At the input, the state has strong multimode spatial correlations: when a photon is detected in any transverse spatial mode $\mathbf{k}$, its twin has a high probability of being detected precisely in the symmetric mode $-\mathbf{k}$ [28]. At the output, the SPAD camera detects photons across all spatial modes in parallel, enabling measurement of both the intensity image (single counts) and the spatially resolved second-order correlation function Γ (coincidence counts) [31]. After propagation, the intensity remains uniform, but a speckle pattern appears in the sum-coordinate projection of Γ, noted Γ^{+} [Fig. 1(f)]. This speckle results from complex two-photon interference [32] and indicates a degradation of the initial strong spatial correlation between the photons. The correlation value between any arbitrary pair of pixels is chosen as the optimization target, and a feedback loop is implemented with an SLM that modulates the wavefront of the input state. If the optimization is successful, a peak emerges in Γ^{+} [Fig. 1(g)].

3. OPTIMIZATION

When a pure two-photon state propagates through a linear scattering medium, the coincidence rate Γ_{kl} between two output modes k and l can be expressed as

$$\Gamma_{kl} = \left| \sum_{m,n} t_{km} t_{ln} \psi_{mn} e^{i\theta_{nm}} \right|^2, \tag{1}$$

where ψ_{mn} is the input two-photon field decomposed over the input modes m and n, t_{kn} is a scattering matrix coefficient linking input mode n to output mode k, and θ_{nm} are adjustable phase terms. In our study, we consider only spatial modes (photons have the same frequency and polarization), though the problem can be generalized to all degrees of freedom. It is clear that a maximum value of Γ_{kl} is reached when all the terms in Eq. (1) are in phase, i.e., when all θ_{nm} are carefully adjusted to cancel the phase of $t_{km} t_{ln} \psi_{mn}$. This problem is analogous to the classical optimization problem detailed in Ref. [1], which is well known to have a unique solution (up to a global phase) with only a global maximum and no local minima, as shown in Fig. 1(d) and demonstrated in Section 1 of Supplement 1. See the Methods section also for details on Eq. (1).

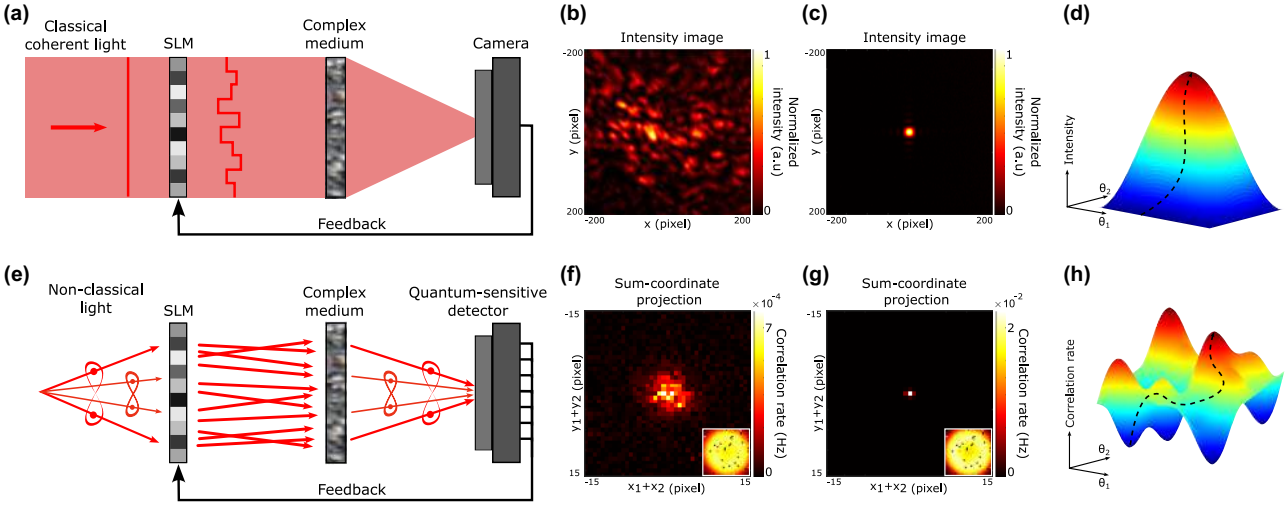

Fig. 1. Classical and non-classical optimizations. (a) Refocusing classical coherent light through a complex medium is achieved by optimization-based wavefront shaping, as described in Ref. [1]. A feedback loop is established between the intensity of the output speckle pattern, measured by a camera, and a spatial light modulator (SLM) that shapes the wavefront of the incident beam. This iterative optimization increases intensity at the target spatial mode, effectively correcting distortions introduced by the medium. (b) and (c) Intensity images measured before and after optimization, respectively. (d) Optimization landscape showing a unique maximum, where θ_1 and θ_2 represent the phases of two SLM pixels. (e) In non-classical optimization, a feedback loop is established between a non-classical property of the quantum state measured at the output and a shaping device at the input. This loop iteratively adjusts the input shaping to enhance the targeted non-classical property. In our experiment, non-classical optimization is implemented using spatially entangled photon pairs propagating through a scattering medium and detected in coincidence using a single-photon avalanche diode (SPAD) camera. Photons are strongly correlated in their momentum, i.e., between $\mathbf{k}$ and $-\mathbf{k}$. (f) Before optimization, the sum-coordinate projection of Γ, noted Γ^{+}, exhibits a speckle pattern, while the intensity is uniform (inset). (g) If the optimization is successful, a peak emerges in Γ^{+}, confirming the restoration of strong spatial correlations between the photons, while the intensity remains uniform (inset). (h) Optimization landscape showing multiple local maxima (up to four; see Section 3 of Supplement 1), where θ_1 and θ_2 represent the phases of two SLM pixels.

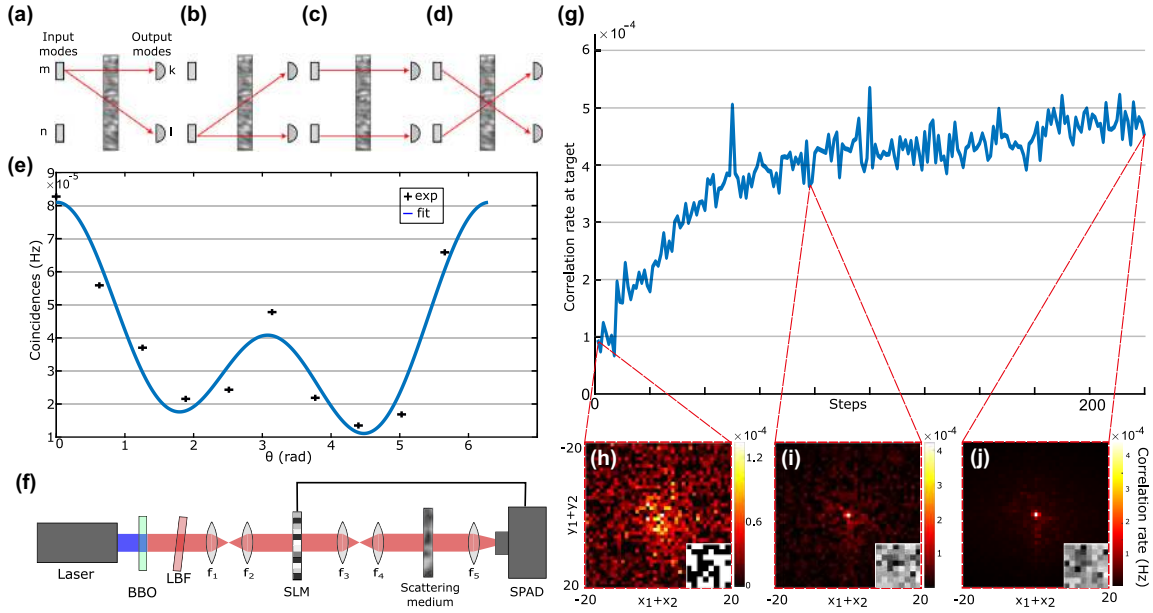

Fig. 2. Optimization results. Four two-photon interference paths occur between two input modes (SLM pixels) and two output modes (SPAD pixels): (a) and (b) Two photons originating from a single input mode m or n and detected at each ouptut modes k and l. (c) Two photons originating from two input modes m and n detected at output modes k and l, and (d) vice versa. (e) Experimental measurement of Γ_{kl} between two arbitrary output modes k and l as a function of the phase θ between the active and reference areas of the SLM. Ten points are measured (black crosses) and fitting the data (blue curve) enables to determine the coefficients $A = 2.21 \cdot 10^{-5}$ Hz, $B = 2.0 \cdot 10^{-5}$ Hz, $C = 3.87 \cdot 10^{-5}$ Hz, $\theta_A = 0.03$ rad, $\theta_B = -0.14$ rad $R^2 = 0.93$) and an optimal phase value of approximately 0.03 rad. (f) A collimated diode laser (405 nm) illuminates β-barium borate (BBO) crystal with a thickness of 0.5 mm to produce spatially entangled pairs of photons by type-I spontaneous parametric down-conversion (SPDC). A long-pass (LPF) positioned after the crystal remove pump photons. Lenses $f_1 - f_2$ image the crystal surface onto a spatial light modulator (SLM), which is itself imaged by lenses $f_3 - f_4$ onto an optical plane where a scattering medium is positioned. The distance between two successive lenses equals the sum of their focal lengths. At the output, a lens f_5 and a single-photon avalanche diode (SPAD) camera positioned in its focal plane collect the photons. A band-pass filter 810 ± 5 nm is positioned in front of the camera (not represented). (g) Optimization curve showing the evolution of the correlation value at the target point as a function of the number of steps taken in the optimization procedure. The enhancement factor is approximately 5. The optimization was performed over 200 steps, corresponding to approximately 120 h. (h)–(j) Γ^+ and SLM phase patterns (insets) at three different steps of the process. More details on the experimental setup can be found in Section 4 of Supplement 1.

For coincidence optimization, unlike the classical case, a single SLM plane does not have enough degrees of freedom to independently control all the θ_{nm} and perfectly align all the terms in Eq. (1). For instance, considering only two spatial input modes (SLM pixels m and n) and two spatial output modes (camera pixels k and l), three terms corresponding to four two-photon paths must be put in phase: $t_{km}t_{lm}\psi_{mm}e^{2i\theta_m}$ [Fig. 2(a)], $t_{ln}t_{kn}\psi_{nn}e^{2i\theta_n}$ [Fig. 2(b)], and $(t_{kn}t_{lm} + t_{km}t_{ln})\psi_{mn}e^{i(\theta_m+\theta_n)}$ [Figs. 2(c) and 2(d)], where θ_m and θ_n are phase shifts applied to modes n and m. When considering $N > 2$ input modes, the optimization problem thus becomes finding a set of phases $\{\theta_n\}$, $n \in [1, N]$, that optimally adjusts the N^2 phases θ_{nm} to maximize the coincidence rate between the target output modes. This optimization problem is significantly more complex than its classical counterpart. For instance, simple simulations shown in Fig. 1(h) and in Section 2 of Supplement 1 demonstrate the presence of local maxima and clearly indicate that the optimal solution is not always unique.

To tackle this problem, we have adapted an iterative optimization approach derived from the random partition algorithm [33]. At each step, a subset of SLM pixels is selected and shifted (active SLM area) relative to another part that remains flat (reference SLM area). The two-photon speckle fields interfere at the output, causing the target coincidence rate Γ_{kl} to vary as

$$\Gamma_{kl}(\theta) = A\cos(2\theta + \theta_A) + B\cos(\theta + \theta_B) + C, \qquad (2)$$

where A, B, C, θ_A, and θ_B are amplitude and phase coefficients that depend on the input two-photon state and scattering matrix, θ is the relative global phase between the active and reference SLM areas, k and l are two arbitrarily chosen output spatial modes with transverse positions (x_k, y_k) and (x_l, y_l). In Eq. (2), the 2θ oscillation arises from the two-photon paths linking one input to two outputs [Figs. 2(a) and 2(b)], while the θ oscillation originates from paths linking two inputs to two outputs [Figs. 2(c)–2(d)]. Figure 2(e) shows an example of Γ_{kl} function of θ measured experimentally using the setup described later in Fig. 2(f). The value of θ maximizing Γ_{kl} is determined by phase-shifting digital holography or by fitting the data with Eq. (2), and is then applied to the pixels in the active area. The algorithm proceeds by selecting and shifting a new subset of pixels at each step, repeating this process until the optimization target no longer evolves. The derivation of Eq. (2) and the search for its optimal phase are detailed in Section 7 (Methods) and Section 3 of Supplement 1.

4. EXPERIMENTAL SETUP

This algorithm is implemented using the experimental setup described in Fig. 2(f). Pairs of photons at 810 nm with the same polarization are generated via type-I spontaneous parametric down-conversion (SPDC) in a thin β-barium borate (BBO) crystal illuminated by a collimated continuous-wave 405 nm laser. The

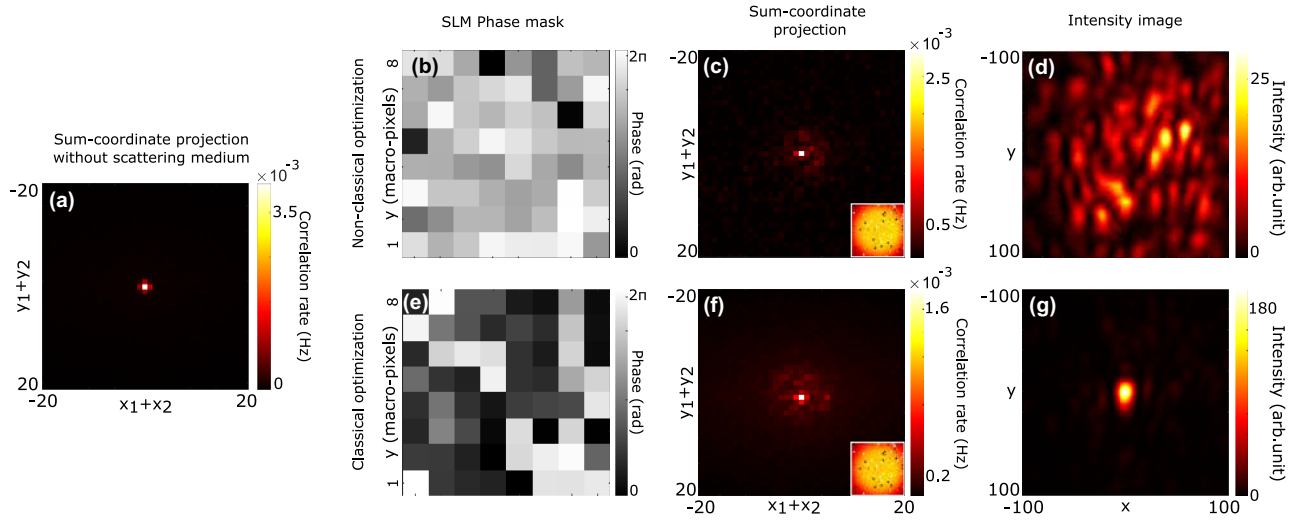

Fig. 3. Focusing results. (a) Sum-coordinate projection acquired without the scattering medium. (b) SLM phase mask and (c) sum-coordinate projection obtained after refocusing spatial correlations through the scattering medium using non-classical optimization with a two-photon entangled state at the input. The output intensity image is shown in the inset. (d) Speckle intensity observed at the output after replacing the two-photon state with classical coherent light. (e) SLM phase mask obtained through classical optimization. (g) In this case, classical light is first refocused in the output intensity. (f) After replacing the classical source with entangled photon pairs, refocusing is then also observed in the sum-coordinate projection. The output intensity image is shown in the inset.

resulting two-photon state is entangled in high spatial dimensions [28]. The crystal output surface is imaged onto an SLM using a $4f$ telescope, which is itself imaged onto an optical plane near where a thin scattering medium (layer of parafilm) is placed. In the SLM plane (input plane), the two-photon wavefunction ψ is characterized experimentally and modeled as a double Gaussian distribution [34,35], with position and momentum correlation widths of $\sigma_{\mathbf{r}} = 2.9 \times 10^{-5}$ m and $\sigma_{\mathbf{k}} = 8.0 \times 10^{2}$ m^{-1}, respectively. At the output, the photons are collected by a lens and a SPAD camera. The optical elements are arranged so that, in the absence of a medium, a Fourier plane of the crystal is imaged onto the SPAD. In this configuration, photons are thus detected in the momentum basis, where they exhibit strong anti-correlations. This is evidenced by the sharp correlation peak in the sum-coordinate projection measured without the medium, shown in Fig. 3(a). Further details on the experimental setup and input state characterization are provided in Section 7 (Methods) and Sections 4 and 5 of Supplement 1.

Figure 2(g) shows an optimization curve obtained by modulating the incident wavefront while monitoring a coincidence target over 200 steps. At the input, the SLM is divided into 8×8 macro-pixels, each 37×37 SLM pixels. At the output, Γ is measured and projected along the sum-coordinate axis to obtain Γ^{+} (see Methods). The optimization target is the coincidence value at an arbitrary pixel T of Γ^{+}. From the SPAD camera perspective, the value Γ^{+}_{T} corresponds to the sum of coincidence rates between all symmetric pixel pairs around a pixel at position (x_T, y_T), i.e., $\Gamma^{+}_{T} = \sum_{k=1}^{M} \Gamma_{T+k,T-k}$, where $T-k$ [resp. $T+k$] corresponds to a pixel at $(x_T - x_k, y_T - y_k)$ [resp. $(x_T + x_k, y_T + y_k)$], and M is the total number of pixels. In our experimental configuration, maximizing Γ^{+}_{T} instead of Γ_{kl} for a given pair of spatial modes k and l has the practical advantage of yielding to stronger signal-to-noise ratio (SNR), while preserving the modulation shape established in Eq. (2), as shown in Section 7 (Methods) and Section 6 of Supplement 1. Simulations shown in Section 9 of Supplement 1 of the paper also present non-classical optimizations performed with Γ_{kl} as the target.

At each optimization step, half of the macropixels are randomly chosen and shifted using 6 or 9 phase increments between 0 and 2π, respectively, for holography or fitting (see Section 7 (Methods) and Section 3 of Supplement 1). Each datapoint in Fig. 2(e) corresponds to a five minute acquisition. Values of Γ^{+}_{T} for different phases θ are then fitted using the model in Eq. (2) to determine the optimal phase shift, which is then applied to the SLM active area. Figures 2(h)–2(j) show the images Γ^{+} at various steps, illustrating the emergence of a peak at the target position, which confirms successful refocusing of photon-pair correlations after the scattering medium. Note that the presented results were obtained by controlling only $8 \times 8 = 64$ input modes, offering a good experimental trade-off between enhancement and acquisition time. As detailed in Ref. [36] and confirmed experimentally in Section 7 of Supplement 1, increasing the number of modes leads to a linear improvement in the enhancement ratio of the final correlation image. However, it also increases the number of steps required for convergence, and thus the total acquisition time. This limitation could be easily mitigated in future implementations by using faster and more efficient coincidence counting cameras, such as the Tpxcam sensor [37,38], as shown in Section 8 of Supplement 1, and advanced optimization algorithms such as genetic approaches [39].

Ultimately, the optimization converges toward the phase mask shown in Fig. 3(b). The focusing peak shown in Fig. 3(c) is approximately five times more intense than the average two-photon speckle surrounding it, while the direct intensity image remains homogeneous (inset). Interestingly, when replacing the photon-pair source with a laser of the same polarization and frequency, we do not observe any refocusing of the classical light in the output intensity image in Fig. 3(d). Instead, a speckled pattern appears. This phase mask thus mitigates scattering for entangled photons but not for classical light.

This result is surprising, in particular when it is compared to the outcome obtained using a classical optimization approach. In this case, the intensity at the center of the output CCD camera is first maximized with the laser at the input using the method of Ref. [1], resulting in an intense peak visible in Fig. 3(g). Then, the classical source is replaced by photon pairs while maintaining the same phase mask on the SLM [Fig. 3(e)]. A peak appears in the sum-coordinate projection in Fig. 3(f), with a value similar to that obtained using the non-classical optimization approach. Non-classical optimization thus converges to phase masks distinct from the classical solution, yet still refocuses entangled photons at the medium output. Additional simulations shown in Sections 9 and 10 of Supplement 1 confirm that these results are reproducible in a range of parameters, including for thicker scattering media (e.g., multiple layers of parafilm stacked together).

5. ROLE OF ENTANGLEMENT

The existence of these "non-classical" solutions, i.e., phase masks that refocus entangled photons without refocusing classical light, is intrinsically linked to the presence of entanglement in the input state. To support this claim, we compare our optimization results with those obtained using non-entangled states. To ensure a meaningful comparison, these separable states are chosen to produce, in the absence of the scattering medium, similar spatial correlations in the camera plane as those observed experimentally with the entangled state. They are described by a density matrix $\rho = \sum_j p_j |\psi^j\rangle\langle\psi^j|$, where $|\psi^j\rangle$ are separable two-photon states of factorizable wavefunction $\psi^j_{nm} = \phi^j_n \chi^j_m$, and p_j its probability. After propagation through the medium, one can show that Eq. (1) simplifies into

$$\Gamma_{kl} = \sum_j p_j \left| \sum_n t_{kn} \phi^j_n e^{i\theta_n} \right|^2 \left| \sum_m t_{lm} \chi^j_m e^{i\theta_m} \right|^2 . \quad (3)$$

In this case, maximizing the correlations between output modes k and l is equivalent to maximizing the sum of output intensity products measured at modes k and l when an ensemble of coherent classical fields, ϕ^j and χ^j, is propagated through the scattering medium. As detailed in Section 7 (Methods) and Section 11 of Supplement 1, we construct two examples of such separable states that reproduce the same sum-coordinate projection as that of the entangled state shown in Fig. 3(a). As detailed in Section 13 and Fig. S13 of Supplement 1, classical-light experiments and simulations show that non-classical optimization can be implemented with these separable states, restoring a correlation peak at the output. Unlike the entangled case, however, a focus also appears at the center of the output classical intensity image, indicating that the optimization consistently converges to the classical solution. Thus, with a non-entangled state, non-classical optimization is equivalent to classical optimization.

However, it is important to note that while entanglement is a necessary condition for reaching a non-classical solution, it is not sufficient. Figure 4 presents simulation results of non-classical optimizations performed with entangled two-photon input states of varying degrees of entanglement. These simulations use the same optical system as described in Fig. 2(f). The degree of entanglement, quantified by the Schmidt number K, is controlled by varying the spatial correlation width $\sigma_\mathbf{r}$ in the SLM plane, while keeping $\sigma_\mathbf{k}$ fixed (see Section 7). In this configuration, all input states produce identical sum-coordinate projections in the absence of scattering, allowing for a consistent basis for comparison. Figure 4 shows the similarity between each classical intensity pattern obtained after non-classical optimization and the one resulting from a direct classical optimization, i.e., a similarity value close to one indicates convergence toward the same solution in both cases. Interestingly, we observe that for values of $\sigma_r > 240$ μm, corresponding to entangled states with $1 < K < 3$, the non-classical optimization converges primarily to the classical solution. This result shows that entanglement alone does not determine the emergence of non-classical solutions.

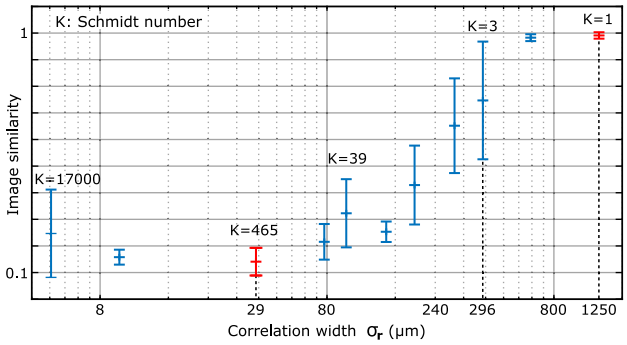

Fig. 4. Non-classical optimizations using entangled states with different degrees of entanglement. Simulation results of non-classical optimization using two-photon states with varying degrees of entanglement. The x-axis indicates the spatial correlation width $\sigma_\mathbf{r}$ in the SLM plane, and the y-axis shows the image similarity (computed using the `corr2` function in MATLAB) between the classical intensity pattern obtained after each non-classical optimization and that of the classical solution. A similarity value close to 1 indicates convergence toward the classical solution, while a significantly lower value indicates a non-classical outcome. For each value of $\sigma_\mathbf{r}$, the optimization is repeated five times, and the error bars represent the standard deviation of the resulting similarity values. The two red datapoints correspond to the experimental cases shown in Figs. 3(b)–3(d) (high-dimensional entangled state, $K = 465$) and Figs. S13 of Supplement 1 (pure separable state, $K = 1$). Selected Schmidt numbers K are indicated above the corresponding points. A transition between convergence to classical and non-classical solutions appears when $\sigma_\mathbf{r}$ exceeds approximately 296, μm, which corresponds to the size of one controlled mode on the SLM (i.e., a macropixel). See Section 7 (Methods) for additional details on the simulations.

In our experiment, the convergence—or not—toward non-classical solutions, particularly the transition observed around $\sigma_r = 240$ μm in Fig. 4, can be qualitatively understood as a competition between first- and second-order coherence of the SPDC light at the input. As discussed in Ref. [40], when the degree of entanglement increases (for a fixed SPDC beam width, set here by $\sigma_\mathbf{k}$), the first-order spatial coherence of the beam decreases. In the high-Schmidt-number regime, first-order coherence is negligible, and the SLM primarily modulates second-order coherence, thereby acting on two-photon interference—the key mechanism responsible for producing non-classical solutions. However, as the Schmidt number decreases, the first-order spatial coherence becomes sufficient for the SLM to influence single-photon interference, steering the optimization toward classical solutions. In Fig. 4, we observe that the transition occurs approximately when $\sigma_\mathbf{r}$ becomes comparable to the SLM macropixel size (i.e., the size of an input mode), approximately 296 μm, which is thus consistent with our interpretation. The ratio between the SLM mode size and the spatial correlation width $\sigma_\mathbf{r}$ at the input plane appears to be a critical parameter governing whether the optimization converges to a classical or non-classical solution. However, while this ratio

plays a major role, other factors such as the specific optimization algorithm or the initial phase mask likely influence the convergence path and the resulting solution type, and would therefore require further investigation to be fully characterized. See Section 14 of Supplement 1 for more details.

6. DISCUSSION

In this work, we implement a non-classical optimization approach using an entangled two-photon state propagating through a scattering medium, using as feedback for the SLM pattern the photon coincidence signal from a SPAD camera. We demonstrate the existence of specific "non-classical" solutions that enable the refocusing of entangled photon pairs without refocusing classical light. Remarkably, these solutions cannot be reached using classical optimization algorithms and have never been observed in previous studies.

We show that the existence of these non-classical solutions is directly linked to the presence of entanglement. Intuitively, this link stems from the ability of entangled states to maintain correlations across multiple measurement bases [41]. During non-classical optimization, the SLM and scattering medium—forming a linear optical system—reconfigure to implement a spatial basis transformation that maximizes correlations. Classically, only a basis that approximates the identity transformation allows refocusing at the output of the medium, as the system effectively tries to make the scattering medium transparent. For entangled states, however, multiple bases become accessible, allowing the system to converge toward one of them, which does not necessarily correspond to the identity. This multiplicity of bases can be interpreted as distinct maxima within a complex optimization landscape. The optimization process may converge to a local maximum when its value is comparable to that of the maximum associated with the classical solution. However, this scenario arises only when the degree of entanglement is sufficiently high, ensuring the existence of multiple alternative bases beyond the identity, i.e., multiple non-classical maxima. In our experimental configuration, our results suggest that a critical parameter governing convergence toward non-classical solutions is the ratio between the size of a controlled SLM input mode and the correlation width $\sigma_{\mathbf{r}}$ in the SLM plane.

In terms of applications, non-classical optimization is primarily a tool that helps mitigate external disturbances to a quantum state, a major challenge in quantum technologies. In optics, this issue arises in various practical scenarios, such as quantum imaging systems affected by optical aberrations [17,42], quantum communication through turbulent atmospheres and fibers [18,23,43], and even quantum computation algorithms where error correction is needed [44]. Beyond that, our approach may also serve as a powerful tool for advancing optical simulation. Recent studies have demonstrated that classical optical optimization techniques can be used to find the ground states of complex physical systems, such as those described by Ising model Hamiltonians [6,45,46]. Solving such problems is known to be computationally hard at a large scale. However, these optical simulators have so far been limited to relatively simple Hamiltonians involving only spin-spin interactions. In contrast, as we show in Section 7 (Methods) and Section 12 of Supplement 1, our system can simulate more complex models described by Hamiltonians that include higher-order multi-spin (more than two) interactions. In this context, non-classical optimization enables the minimization of the system energy to identify its ground state. For example, this is demonstrated experimentally in Fig. S12 of Supplement 1, where we simulate a 64-spin system governed by a Hamiltonian containing two-spin, three-spin, and four-spin interactions, a level of complexity not accessible to classical optical Ising machines. With further developments in programmability and improved convergence speed, our non-classical optimization framework can also become a new tool for solving new classes of computationally hard problems.

7. METHODS

A. Details on Equation (1)

Considering photons degenerate in frequency and polarization, a pure two-photon state is expressed as

$$|\Psi\rangle = \iint \psi(\mathbf{r_1}, \mathbf{r_2}) a^\dagger_{\mathbf{r_1}} a^\dagger_{\mathbf{r_2}} \mathrm{d}\mathbf{r_1}\mathrm{d}\mathbf{r_2}|0\rangle, \tag{4}$$

where $a^\dagger_{\mathbf{r_1}}$ is the photon creation operator in the spatial mode $\mathbf{r_1}$, and $\psi(\mathbf{r_1}, \mathbf{r_2})$ represents the spatial two-photon wavefunction. After propagation through a linear optical system characterized by a coherent point spread function $t(\mathbf{r}', \mathbf{r})$, where $\mathbf{r}$ and $\mathbf{r}'$ denote transverse positions in the input and output planes, respectively, the output two-photon wavefunction, noted ψ', becomes [47]

$$\psi'(\mathbf{r}'_1, \mathbf{r}'_2) = \iint \psi(\mathbf{r_1}, \mathbf{r_2}) t(\mathbf{r}'_1, \mathbf{r_1}) t(\mathbf{r}'_2, \mathbf{r_2}) \mathrm{d}\mathbf{r_1}\mathrm{d}\mathbf{r_2}. \tag{5}$$

The spatial second-order correlation function Γ is defined as the squared absolute value of the corresponding two-photon wavefunction, i.e., $\Gamma(\mathbf{r_1}, \mathbf{r_2}) = |\psi(\mathbf{r_1}, \mathbf{r_2})|^2$. Equation (1) is thus derived by discretizing Eq. (5). Specifically, in the discretized representation, the function $t(\mathbf{r}', \mathbf{r})$ corresponds to the scattering matrix t_{kl}, where l labels an input pixel on the spatial light modulator (SLM) and k labels an output pixel on the camera.

B. Details on Equation (2)

Considering two output modes k and l and two SLM areas, denoted $\mathcal{M}$ and $\mathcal{N}$ (active and reference areas), the coincidence rate Γ_{kl} results from the coherent sum of complex terms associated with the two-photon interference processes shown in Figs. 2(a)–2(d):

$$\Gamma_{kl} = \left| e^{2i\theta_{\mathcal{M}}} S_{\mathcal{M}} + e^{2i\theta_{\mathcal{N}}} S_{\mathcal{N}} + e^{i(\theta_{\mathcal{M}}+\theta_{\mathcal{N}})} S_{\mathcal{M},\mathcal{N}} \right|^2, \tag{6}$$

where $\theta_{\mathcal{M}}$ and $\theta_{\mathcal{N}}$ are the phases of the active and reference areas and

$$S_{\mathcal{M}} = \sum_{m\in\mathcal{M}} t_{km} t_{lm} \psi_{mm}, \tag{7}$$

$$S_{\mathcal{N}} = \sum_{n\in\mathcal{N}} t_{kn} t_{ln} \psi_{nn}, \tag{8}$$

$$S_{\mathcal{M},\mathcal{N}} = \sum_{m\in\mathcal{M}, n\in\mathcal{N}} [t_{kn} t_{lm} + t_{km} t_{ln}] \psi_{mn}. \tag{9}$$

Expanding Eq. (6) leads to

$$\Gamma_{kl} = |S_{\mathcal{M}}|^2 + |S_{\mathcal{N}}|^2 + |S_{\mathcal{M},\mathcal{N}}|^2 + e^{2i(\theta_{\mathcal{M}}-\theta_{\mathcal{N}})} S_{\mathcal{M}} S^*_{\mathcal{N}} + e^{-2i(\theta_{\mathcal{M}}-\theta_{\mathcal{N}})} S^*_{\mathcal{M}} S_{\mathcal{N}} + e^{i(\theta_{\mathcal{M}}-\theta_{\mathcal{N}})} S_{\mathcal{M}} S^*_{\mathcal{M},\mathcal{N}} + e^{-i(\theta_{\mathcal{M}}-\theta_{\mathcal{N}})} S^*_{\mathcal{M}} S_{\mathcal{M},\mathcal{N}} + e^{i(\theta_{\mathcal{N}}-\theta_{\mathcal{M}})} S_{\mathcal{N}} S^*_{\mathcal{M},\mathcal{N}} + e^{-i(\theta_{\mathcal{N}}-\theta_{\mathcal{M}})} S^*_{\mathcal{N}} S_{\mathcal{M},\mathcal{N}}. \quad (10)$$

By identifying the coefficients of Eq. (10) with those of Eq. (2), we find

$$\theta = \theta_{\mathcal{M}} - \theta_{\mathcal{N}}, \quad (11)$$

$$A = 2|S_{\mathcal{M}} S^*_{\mathcal{N}}|, \quad (12)$$

$$\theta_A = \arg(S_{\mathcal{M}} S^*_{\mathcal{N}}), \quad (13)$$

$$B = 2|S_{\mathcal{M}} S^*_{\mathcal{M},\mathcal{N}} + S_{\mathcal{N}} S^*_{\mathcal{M},\mathcal{N}}|, \quad (14)$$

$$\theta_B = \arg(S_{\mathcal{M}} S^*_{\mathcal{M},\mathcal{N}} + S_{\mathcal{N}} S^*_{\mathcal{M},\mathcal{N}}), \quad (15)$$

$$C = |S_{\mathcal{M}}|^2 + |S_{\mathcal{N}}|^2 + |S_{\mathcal{M},\mathcal{N}}|^2. \quad (16)$$

C. Determination of the Optimal Phase

Determining the value of θ that maximizes Γ at each optimization step is done in two stages. First, the coefficients A, B, C, θ_A, and θ_B are determined by measuring Γ for six phase values $\{0, \pi/4, \pi/2, \pi, 3\pi/2, 5\pi/4\}$ as follows:

$$Be^{i\theta_B} = \frac{\Gamma(0) - \Gamma(\pi)}{2} + i\frac{\Gamma(3\pi/2) - \Gamma(\pi/2)}{2}, \quad (17)$$

$$C = \frac{\Gamma(0) + \Gamma(\pi) + \Gamma(3\pi/2) + \Gamma(\pi/2)}{4}, \quad (18)$$

$$Ae^{i\theta_A} = \frac{\Gamma(0) + \Gamma(\pi) - 2C}{2} + i\frac{\Gamma(\pi/4) + \Gamma(5\pi/4) - 2C}{2}. \quad (19)$$

To reduce uncertainty due to measurement noise, one can also measure more than six points and fit them to the model of Eq. (2) by minimizing the sum of squared errors. Once the coefficients are known, the optimal value of θ is determined analytically by solving a fourth-degree polynomial equation or using a numerical approach. More details can be found in Section 3 of Supplement 1.

D. Modeling and Characterization of the Two-Photon Entangled State

In the SLM plane, the two-photon wavefunction ψ is modeled by a double Gaussian distribution [34,35]:

$$\psi(\mathbf{r_1}, \mathbf{r_2}) = A \exp\left\{-\frac{|\mathbf{r_1} - \mathbf{r_2}|^2}{4\sigma_{\mathbf{r}}^2}\right\} \exp\left\{-\frac{|\mathbf{r_1} + \mathbf{r_2}|^2 \sigma_{\mathbf{k}}^2}{4}\right\}, \quad (20)$$

where A is a normalization factor, $\mathbf{r_1}$ and $\mathbf{r_2}$ are the idler and signal photons' transverse positions in the SLM plane, and $\sigma_{\mathbf{r}}$ and $\sigma_{\mathbf{k}}$ are the position and momentum correlation widths, respectively. To determine their values, the SPAD camera was replaced by an electron multiplied charge coupled device camera (EMCCD) to have a better pixel resolution, and the method detailed in Refs. [48,49] was used. The values $\sigma_{\mathbf{r}} = 2.9 \times 10^{-5}$ m and $\sigma_{\mathbf{k}} = 8.0 \times 10^{2}$ m^{-1} were found. See Section 5 of Supplement 1 for more details.

E. Measurement of Γ and Sum-Coordinate Projection Γ^+

The spatially resolved second-order correlation function Γ_{kl}, where k and l are two pixels of the SPAD camera centered at transverse positions (x_k, y_k) and (x_l, y_l), is measured by acquiring a set of $P+1$ frames $\{I^{(p)}\}_{p\in[[1,P+1]]}$ using a fixed exposure time and processing them using the formula [31,50]:

$$\Gamma_{kl} = \frac{1}{P}\sum_{p=1}^{P}\left[I_k^{(p)} I_l^{(p)} - I_k^{(p)} I_l^{(p+1)}\right]. \quad (21)$$

Because the SPAD camera does not resolve the number of photons, photon coincidences at the same pixel (i.e., coefficients Γ_{kk}) cannot be measured, and are therefore set to zero. Additionally, correlation values between neighboring pixels suffer from cross-talk and must be corrected, as detailed in Ref. [21]. The sum-coordinate projection of Γ is then calculated using the following formula:

$$\Gamma_T^+ = \sum_{k=1}^{M} \Gamma_{T-k,k}, \quad (22)$$

where $T-k$ denotes camera pixels of transverse position $(x_T - x_k, y_T - y_k)$. Using a continuous-variable formalism, this definition becomes

$$\Gamma^+(\mathbf{r_T}) = \int \Gamma(\mathbf{r_T} - \mathbf{r}, \mathbf{r})\mathrm{d}\mathbf{r}, \quad (23)$$

where $\mathbf{r_T} = (x_T, y_T)$ is the transverse position of the target.

F. Optimization Target

In our experiment, we chose to use Γ_T^+ as the optimization target instead of Γ_{kl} directly. This choice was motivated by practical considerations: the SNR is higher for Γ_T^+ than for Γ_{kl}. Indeed, Eq. (22) shows that Γ_T^+ results from a sum of many Γ_{kl} terms. If each term is noisy (i.e., $\Gamma_{kl} + \epsilon_{kl}$, with independent noise ϵ_{kl}), then the variance of the resulting noise on Γ_T^+ is proportional to the number of nonzero terms in the sum. Since the signal values add directly, the overall SNR is higher on average by the square-root of the number of terms. Furthermore, it is important to note that the form of Eq. (2), originally derived for Γ_{kl}, is preserved under summation. The resulting function Γ_T^+ can thus also be expressed as $A\cos(2\theta + \theta_A) + B\cos(\theta + \theta_B) + C$, where the different parameters are combinations of those associated with the individual terms in the sum. This choice of target and experimental configuration makes the experiment feasible with current detection technologies while maintaining the general applicability of our approach. Additional details are provided in Section 6 of Supplement 1.

G. Construction of the Non-Entangled States

We describe here the two non-entangled states used to compare with the entangled-state non-classical optimization. The first non-entangled state chosen is a pure separable state, defined by its wavefunction $\psi(\mathbf{r_1}, \mathbf{r_2}) = \phi(\mathbf{r_1})\chi(\mathbf{r_2})$. To reproduce the same sum-coordinate projection Γ^+ as that of the entangled state measured on the camera without the scattering medium, i.e., a Gaussian with width proportional to $\sigma_\mathbf{k}$ shown in Fig. 3(a), the individual wavefunctions in the SLM plane are chosen as

$$\phi(\mathbf{r}) = \chi(\mathbf{r}) = A' \exp\left\{-\frac{|\mathbf{r}|^2\sigma_\mathbf{k}^2}{8}\right\}, \tag{24}$$

where A is a normalization constant.

The second non-entangled state chosen is a mixed separable state, denoted ρ. In this case, one can choose the weights p_j and the wavefunctions ϕ^j and χ^j to exactly reproduce the full second-order correlation function Γ measured in the camera plane for the entangled state without the medium—and consequently also Γ^+. For that, ρ is defined using continuous-variable formalism as $\rho = \int\int p_\mathbf{q} |\psi^\mathbf{q}\rangle\langle\psi^\mathbf{q}| \mathrm{d}\mathbf{q}$, where

$$\phi^\mathbf{q}(\mathbf{r_1}) = \exp\left\{-\frac{|\mathbf{r_1}|^2\sigma_\mathbf{k}^2}{4(1+\sigma_\mathbf{r}^2\sigma_\mathbf{k}^2)}\right\} e^{-i\mathbf{q}\mathbf{r_1}}, \tag{25}$$

$$\chi^\mathbf{q}(\mathbf{r_2}) = e^{-i\mathbf{q}\mathbf{r_2}}, \tag{26}$$

$$p_\mathbf{q} = D, \tag{27}$$

where $\psi^\mathbf{q}(\mathbf{r_1})\chi^\mathbf{q}(\mathbf{r_2})$ is the (factorizable) two-photon function of the state $|\psi^\mathbf{q}\rangle$, and D is a constant chosen to ensure proper normalization of the state. More details about these states and the non-classical optimization performed with them are provided in Sections 11 and 13 of Supplement 1.

H. Details on the Simulations

The simulations presented in Fig. 4 of this paper and Figs. S13(e)–S13(h) of Supplement 1 were performed by propagating the two-photon state through the optical system using matrix multiplication in MATLAB. In Figs. S13(e)–13(h) of Supplement 1, the scattering matrix was generated from a random phase mask followed by a Fourier transform, producing a disordered medium with statistical properties similar to those observed experimentally. The state ρ was generated according to the model defined in Eqs. (25), (26), and (27), using the experimentally measured values of $\sigma_\mathbf{k}$ and $\sigma_\mathbf{x}$ to closely match the characteristics of the entangled state and the optical setup. In contrast, for Fig. 4, the scattering matrix was measured experimentally using the method described in Ref. [26]. The spatial correlation width in the SLM plane, $\sigma_\mathbf{r}$, was varied from 1.6 μm to 1250 μm, while $\sigma_\mathbf{k}$ was held constant. The Schmidt number K was then calculated using the expression $K = \frac{1}{4}(\sigma_\mathbf{r}\sigma_\mathbf{k} + (\sigma_\mathbf{r}\sigma_\mathbf{k})^{-1})^2$ [34,35]. Further details on the simulation methods are provided in Sections 2 and 9 of Supplement 1.

I. Energy Minimization of a Multi-Spin Hamiltonian

To use our system as an optical simulator, we associate each input mode n of the SLM (macropixel) with a spin variable σ_n. The value of this spin, either $+1$ or -1, is defined by the square of the phase shift applied to the input mode, which can therefore take physical values of 0 or $\pi/2$. After propagation through the scattering medium, the correlation value Γ_T^+ depends on the phase values applied by all the macropixels on the SLM. This value is then identified with the energy of a multi-spin interaction Hamiltonian of the following form:

$$H(\sigma) = -\frac{1}{2}\sum_{nm} J_{nm}^T \sigma_n\sigma_m - \frac{1}{2}\sum_{nml} \Lambda_{nml}^T \sigma_n\sigma_m\sigma_l - \frac{1}{2}\sum_{nmlp} Q_{nmlp}^T \sigma_n\sigma_m\sigma_l\sigma_p - \frac{1}{2}\sum_n K_n^T\sigma_n, \tag{28}$$

where the coefficients K_n^T, J_{nm}^T, Λ_{nml}^T, and Q_{nmlp}^T depend on the transmission matrix elements, the input two-photon wavefunction, the macropixel size of the SLM, and the optimization target T. Notably, this Hamiltonian includes three-spin and four-spin interaction terms. To find its ground state, we perform a non-classical optimization on Γ_T^+, constrained to phase values of 0 or $\pi/2$ on the SLM macropixels. Figure S12 of Supplement 1 shows an example of such an optimization implemented with $8 \times 8 = 64$ spins, which converges toward a minimum energy configuration. The resulting SLM pattern—i.e., the set of 8×8 spin values—represents the ground state of the system, found with an estimated accuracy of 25% due to noise limitations. Further details on this optical simulation, including the derivation of Eq. (28) and the full expressions of the parameters K_n^T, J_{nm}^T, Λ_{nml}^T, and Q_{nmlp}^T, are provided in Section 12 of Supplement 1.

Funding. European Research Council (SQMIC-101039375); Agence Nationale de la Recherche (ANR-24-CE97-0001, ANR-23-CE47-0014); Royal Academy of Engineering (EP/Y029097/1, EP/Z533166/1).

Acknowledgment. B. Courme analyzed the data, designed and performed the experiment, with support from C. Vernière and M. Joly. H. Defienne acknowledges fundings from the European Research Council and Agence Nationale de Recherche. H. Defienne, D. Faccio, and S. Gigan conceived the original idea and supervised the project. All authors discussed the results and contributed to the paper. DF acknowledges financial support from the Royal Academy of Engineering under the Chairs in Emerging Technology and Research Fellowships scheme and the U.K. Engineering and Physical Sciences Research Council (Grants No. EP/Y029097/1, EP/Z533166/1).

Disclosures. The authors declare no conflicts of interest.

Data availability. Data underlying the results presented in this paper are not publicly available at this time but may be obtained from the authors upon reasonable request.

Supplemental document. See Supplement 1 for supporting content.

REFERENCES

1. I. M. Vellekoop and A. P. Mosk, "Focusing coherent light through opaque strongly scattering media," Opt. Lett. **32**, 2309–2311 (2007).
2. R. Horstmeyer, H. Ruan, and C. Yang, "Guidestar-assisted wavefront-shaping methods for focusing light into biological tissue," Nat. Photonics **9**, 563–571 (2015).
3. S. Gigan, O. Katz, H. B. d. Aguiar, *et al.*, "Roadmap on wavefront shaping and deep imaging in complex media," J. Phys. Photonics **4**, 042501 (2022).

4. T. Čižmár and K. Dholakia, "Shaping the light transmission through a multimode optical fibre: complex transformation analysis and applications in biophotonics," Opt. Express **19**, 18871–18884 (2011).
5. M. A. Taylor, M. Waleed, A. B. Stilgoe, *et al.*, "Enhanced optical trapping via structured scattering," Nat. Photonics **9**, 669–673 (2015).
6. D. Pierangeli, M. Rafayelyan, C. Conti, *et al.*, "Scalable spin-glass optical simulator," Phys. Rev. Appl. **15**, 034087 (2021).
7. M. Leonetti, E. Hörmann, L. Leuzzi, *et al.*, "Optical computation of a spin glass dynamics with tunable complexity," Proc. Natl. Acad. Sci. **118**, e2015207118 (2021).
8. O. Lib and Y. Bromberg, "Quantum light in complex media and its applications," Nat. Phys. **18**, 986–993 (2022).
9. T. J. Huisman, S. R. Huisman, A. P. Mosk, *et al.*, "Controlling single-photon Fock-state propagation through opaque scattering media," Appl. Phys. B **116**, 603–607 (2014).
10. H. Defienne, M. Barbieri, B. Chalopin, *et al.*, "Nonclassical light manipulation in a multiple-scattering medium," Opt. Lett. **39**, 6090–6093 (2014).
11. T. A. W. Wolterink, R. Uppu, G. Ctistis, *et al.*, "Programmable two-photon quantum interference in 103 channels in opaque scattering media," Phys. Rev. A **93**, 053817 (2016).
12. J. Carpenter, B. J. Eggleton, and J. Schröder, "110 × 110 optical mode transfer matrix inversion," Opt. Express **22**, 96–101 (2014).
13. H. Defienne, M. Barbieri, I. A. Walmsley, *et al.*, "Two-photon quantum walk in a multimode fiber," Sci. Adv. **2**, e1501054 (2016).
14. S. Leedumrongwatthanakun, L. Innocenti, H. Defienne, *et al.*, "Programmable linear quantum networks with a multimode fibre," Nat. Photonics **14**, 139–142 (2020).
15. S. Goel, S. Leedumrongwatthanakun, N. H. Valencia, *et al.*, "Inverse design of high-dimensional quantum optical circuits in a complex medium," Nat. Phys. **20**, 232–239 (2024).
16. A. Makowski, M. Dąbrowski, I. M. Antolovic, *et al.*, "Large reconfigurable quantum circuits with SPAD arrays and multimode fibers," Optica **11**, 340–343 (2024).
17. P. Cameron, B. Courme, C. Vernière, *et al.*, "Adaptive optical imaging with entangled photons," Science **383**, 1142–1148 (2024).
18. N. H. Valencia, S. Goel, W. McCutcheon, *et al.*, "Unscrambling entanglement through a complex medium," Nat. Phys. **16**, 1112–1116 (2020).
19. O. Lib, G. Hasson, and Y. Bromberg, "Real-time shaping of entangled photons by classical control and feedback," Sci. Adv. **6**, eabb6298 (2020).
20. F. Devaux, A. Mosset, S. M. Popoff, *et al.*, "Restoring and tailoring very high dimensional spatial entanglement of a biphoton state transmitted through a scattering medium," J. Opt. **25**, 055201 (2023).
21. B. Courme, P. Cameron, D. Faccio, *et al.*, "Manipulation and certification of high-dimensional entanglement through a scattering medium," PRX Quantum **4**, 010308 (2023).
22. R. Shekel, O. Lib, and Y. Bromberg, "Shaping entangled photons through arbitrary scattering media using an advanced wave beacon," Opt. Quantum **2**, 303–309 (2024).
23. M. T. Gruneisen, M. L. Eickhoff, S. C. Newey, *et al.*, "Adaptive-optics-enabled quantum communication: a technique for daytime space-to-Earth links," Phys. Rev. Appl. **16**, 014067 (2021).
24. J. Zhao, Y. Zhou, B. Braverman, *et al.*, "Performance of real-time adaptive optics compensation in a turbulent channel with high-dimensional spatial-mode encoding," Opt. Express **28**, 15376–15391 (2020).
25. L. Scarfe, F. Hufnagel, M. F. Ferrer-Garcia, *et al.*, "Fast adaptive optics for high-dimensional quantum communications in turbulent channels," arXiv (2023).
26. S. M. Popoff, G. Lerosey, R. Carminati, *et al.*, "Measuring the transmission matrix in optics: an approach to the study and control of light propagation in disordered media," Phys. Rev. Lett. **104**, 100601 (2010).
27. C. Stockbridge, Y. Lu, J. Moore, *et al.*, "Focusing through dynamic scattering media," Opt. Express **20**, 15086–15092 (2012).
28. S. P. Walborn, C. Monken, S. Pádua, *et al.*, "Spatial correlations in parametric down-conversion," Phys. Rep. **495**, 87–139 (2010).
29. H. Defienne, M. Reichert, and J. W. Fleischer, "Adaptive quantum optics with spatially entangled photon pairs," Phys. Rev. Lett. **121**, 233601 (2018).
30. J. R. Ott, N. A. Mortensen, and P. Lodahl, "Quantum interference and entanglement induced by multiple scattering of light," Phys. Rev. Lett. **105**, 090501 (2010).
31. B. Ndagano, H. Defienne, A. Lyons, *et al.*, "Imaging and certifying high-dimensional entanglement with a single-photon avalanche diode camera," Npj Quantum Inf. **6**, 1–8 (2020).
32. W. Peeters, J. Moerman, and M. Van Exter, "Observation of two-photon speckle patterns," Phys. Rev. Lett. **104**, 173601 (2010).
33. I. M. Vellekoop and A. Mosk, "Phase control algorithms for focusing light through turbid media," Opt. Commun. **281**, 3071–3080 (2008).
34. M. V. Fedorov, Y. M. Mikhailova, and P. A. Volkov, "Gaussian modelling and Schmidt modes of SPDC biphoton states," J. Phys. B At. Mol. Opt. Phys. **42**, 175503 (2009).
35. J. Schneeloch and J. C. Howell, "Introduction to the transverse spatial correlations in spontaneous parametric down-conversion through the Biphoton Birth Zone," J. Opt. **18**, 053501 (2016).
36. R. Shekel, S. M. Popoff, and Y. Bromberg, "Fundamental bounds of wavefront shaping of spatially entangled photons," arXiv (2025).
37. A. Nomerotski, "Imaging and time stamping of photons with nanosecond resolution in Timepix based optical cameras," Nucl. Instrum. Methods Phys. Res. Sect. A **937**, 26–30 (2019).
38. B. Courme, C. Vernière, P. Svihra, *et al.*, "Quantifying high-dimensional spatial entanglement with a single-photon-sensitive time-stamping camera," Opt. Lett. **48**, 3439 (2023).
39. D. B. Conkey, A. N. Brown, A. M. Caravaca-Aguirre, *et al.*, "Genetic algorithm optimization for focusing through turbid media in noisy environments," Opt. Express **20**, 4840–4849 (2012).
40. B. E. A. Saleh, A. F. Abouraddy, A. V. Sergienko, *et al.*, "Duality between partial coherence and partial entanglement," Phys. Rev. A **62**, 043816 (2000).
41. C. Spengler, M. Huber, S. Brierley, *et al.*, "Entanglement detection via mutually unbiased bases," Phys. Rev. A **86**, 022311 (2012).
42. B. Freitas, Y. Zhang, D. England, *et al.*, "Quantum correlated image recording through noisy and turbulent channels," Opt. Quantum **3**, 78–83 (2024).
43. V. M. Acosta, D. Dequal, M. Schiavon, *et al.*, "Analysis of satellite-to-ground quantum key distribution with adaptive optics," New J. Phys. **26**, 023039 (2024).
44. M. Müller, A. Rivas, E. Martínez, *et al.*, "Iterative phase optimization of elementary quantum error correcting codes," Phys. Rev X **6**, 031030 (2016).
45. D. Pierangeli, G. Marcucci, and C. Conti, "Large-scale photonic ising machine by spatial light modulation," Phys. Rev. Lett. **122**, 213902 (2019).
46. D. Veraldi, D. Pierangeli, S. Gentilini, *et al.*, "Fully programmable spatial photonic ising machine by focal plane division," Phys. Rev. Lett. **134**, 063802 (2025).
47. A. F. Abouraddy, B. E. A. Saleh, A. V. Sergienko, *et al.*, "Entangled-photon Fourier optics," J. Opt. Soc. Am. B **19**, 1174–1184 (2002).
48. P.-A. Moreau, J. Mougin-Sisini, F. Devaux, *et al.*, "Realization of the purely spatial Einstein-Podolsky-Rosen paradox in full-field images of spontaneous parametric down-conversion," Phys. Rev. A **86**, 010101 (2012).
49. M. P. Edgar, D. S. Tasca, F. Izdebski, *et al.*, "Imaging high-dimensional spatial entanglement with a camera," Nat. Commun. **3**, 984 (2012).
50. H. Defienne, M. Reichert, and J. W. Fleischer, "General model of photon-pair detection with an image sensor," Phys. Rev. Lett. **120**, 203604 (2018).